IUTAM Symposium Wind Waves, 4-8 September 2017, London, UK

Detailed measurements of interfacial dynamics in air-water pipe flow

A.A. Ayati, P. Vollestad, A. Jensen

Department of Mathematics, University of Oslo, N-0316 Oslo, Norway

Abstract

Stratified air-water flow in a horizontal pipe is investigated experimentally using particle image velocimetry and conductance probes. This flow regime is characterized by a complex interplay between a turbulent airflow and propagating waves at the interface. The waves are generated by interfacial shear and pressure forces exerted by the faster flowing airflow. The goal of this study is to characterize the waves by means of statistical and spectral methods, and to explore the influence of different wave regimes on the airflow.

Two cases in which the air bulk velocity increases from 2.4 m/s (case A) to 3.5 m/s (case B), while the liquid velocity remains constant at 0.26 m/s, are assessed in detail. Case A belongs to a region of flow conditions in which wave amplitudes grow as a consequence of increasing gas flow rates, i.e., wave growth regime. Meanwhile, case B is in a regime of saturated wave amplitudes. In the first case, the interface was populated by small amplitude 2D waves of relatively small steepness ($ak \approx 0.07$). These waves obey Gaussian statistics and are thus considered to be linear. In the second case, the waves are larger, steeper ($ak \approx 0.13$) and considerably more irregular. They display non-linear behaviour (steep crests and long troughs) and their exceedance probability distribution deviates significantly from Gaussian statistics. Bicoherence maps show evidence of both overtone and sub-harmonic interactions.

Airflow velocity fields acquired by PIV were subjected to a conditional phase-averaging method based on a steepness criterion. The phase-averaged vorticity field shows evidence of shear-layer separation above the steeper waves of case B. Hence, in addition to non-linear mode interactions and micro-breaking, shear-layer separation may contribute to the transition from the growth regime to the saturation regime.

1. Introduction

Gas-liquid flow in pipes is relevant to a variety of industrial applications, ranging from nuclear and petroleum industries to waste water mains [32, 37, 16]. Inside natural gas pipelines, the flow often consists of both a gaseous and a liquid phase, in the form of gas-water or gas-condensate combination. Both phases are usually turbulent and flow in the same direction. Generally, the gaseous phase flows significantly faster than the liquid phase giving rise

---

* Corresponding author. Tel.: +47-22855988
  E-mail address: awalaa@math.uio.no

to waves at the interface which separates the two fluids. It is known that the presence of interfacial waves enhances drag between the phases, and consequently increases the pressure drop [4]. For this reason, there have been intense efforts, within multiphase flow research, to build models that are able to accurately predict the pressure drop, among other important system parameters. The most common modelling approach related to this problem has been based on the use of semi-empirical correlations for the interfacial friction factor. Since this approach is very system dependent, significant discrepancies in proposed correlations are found in the literature, see for instance [38, 3, 43].

Another issue related to this flow takes place at high flow rates. Under such conditions, the interfacial waves may grow to block the pipe cross-section and onset slug flow, i.e., an intermittent flow regime which induces large pressure fluctuations in the system. This flow regime can be detrimental to pipelines as well as their supporting infrastructure. Transition to slug flow, which is a direct consequence of the confined pipe geometry, represents one of the major differences between gas-liquid flow in pipes and open wind-wave systems. Accurate prediction of this flow regime transition is yet another important motivation for two-phase pipe flow research. In the framework of the one-dimensional two-fluid model [40], this transition has traditionally been modelled using a viscous Kelvin Helmholtz approach [10, 42]. More recent approaches consist of solving the two-dimensional Orr-Sommerfeld eigenvalue problem [30, 9], and including weakly non-linear wave interaction [19]. Although some of these approaches are sophisticated, there is still no consensus regarding the solution of this problem as predictions fail to accurately reproduce experimental results, see [33] for a review.

At lower flow rates, beneath the conditions for slug onset, the small-scale dynamics that govern the interfacial region in gas-liquid pipe flow are reminiscent of open wind-wave systems. Interfacial perturbations are excited at the inlet region of the pipe by means of turbulent pressure fluctuations in the airflow [36] and/or shear-instabilities. Once present, these perturbations grow with fetch, most likely as a result of Miles's mechanism [34], and become gravity-capillary waves. Further downstream, the waves interact with each other, both linearly and non-linearly, depending on the flow rates. The non-linear interactions appear first as sub-harmonic bifurcation, i.e., period doubling [27, 14]. Even further downstream, the waves may reach a state of equilibrium between energy input from the airflow and dissipation due to viscous effects, wave breaking and non-linear energy transfer towards stable modes [29]. The flow is then considered as fully developed and the wave amplitudes remain more or less constant even with increasing the airflow forcing.

In their study of interfacial gravity-capillary waves in horizontal gas-liquid flows, Jurman et al. [29] pointed out non-linear modal interactions as the main mechanism for the observed amplitude saturation. However, their study did not include any investigation of the momentum input source, i.e., the airflow. Numerous subsequent studies, both experimental and numerical [45, 23, 44, 17] have reported evidence of intermittent flow separation events above relatively steep non-breaking waves. Such events are believed to reduce the momentum transfer from the airflow to the waves as the contact surface between the phases diminishes. Therefore, this mechanism should probably be considered as yet another contributor to the transition to the saturated regime.

The complexity of the system under investigation lies in the fact that all above mentioned mechanisms take place simultaneously. Furthermore, the circular pipe geometry certainly adds complexity, in ways that have not yet been fully understood. Thus, there is still a need for conducting phenomenological studies such as the present one, in order to identify and quantify the various mechanisms that govern the fully stratified flow regime.

The specific aim of this paper is to address interfacial mode interaction and airflow separation by, firstly, characterizing the interfacial waves through statistical and spectral methods, and secondly, use PIV measurements to explore the effect of different wave regimes on the airflow structure. Two cases are depicted amongst a larger set in which the liquid flow rate is kept constant while the gas superficial velocity increases from approx. 1 m/s to 4 m/s. These cases lie in two observed regimes, i) wave growth and ii) wave saturation regime. Note that all measurements are acquired at a single position approximately 25 m (250D) downstream of the inlet, at which the flow is considered to be fully developed.

This manuscript is organized in the following manner. After this short introduction, the experimental set-up and methodology are described in section 2. The latter consists of a zero-crossing analysis of wave probe signals as well as a phase-averaging procedure applied on airflow PIV velocity fields. The results are then presented in section 3. These consist of i) a characterization of interfacial wave regime through the assessment of exceedance probability distributions, power spectra and bicoherence plots, and ii) a presentation of the phase-averaged airflow velocity and

vorticity fields with emphasis on shear-layer separation above steep waves. Finally, concluding remarks are presented in section 4.

2. Experimental set-up and methodology

Experiments were conducted at the Hydrodynamic Laboratory, University of Oslo. The laboratory has a 31 m long horizontal acrylic pipe with internal diameter D=10 cm. The test fluids were air and water at atmospheric pressure. Both fluids were introduced at the pipe inlet using a frequency-regulated pump and fan, for the water and air, respectively. The water and air mass flow rates were measured with an Endress Hauser Promass and an Emerson MicroMotion Coriolis flow meter, with 0.2 % and 0.05 % of maximum measured values in accuracy, respectively. A schematic view of the pipe-loop is shown in figure 1.

During the experimental campaign, three experimental techniques were employed; i) Simultaneous Two-Phase Particle Image Velocimetry (PIV), ii) Conductance Probes (CP) and iii) Hot-Wire (HW) anemometry. However, in this paper, only data acquired by PIV and conductance probes will be assessed. The PIV set-up was located 26m (260D) downstream of the pipe inlet. It provided velocity fields in the pipe centre plane in both the gaseous and liquid phase simultaneously using two cameras with high spatial resolution and one high-energy Nd:YAG laser. Small water droplets ($\bar{d} \sim 6\mu$m) were introduced at the pipe inlet as tracers in the airflow, whilst the water flow was seeded with commercial spherical polyamide particles ($\bar{d} \sim 50\mu$m). It should be emphasised that only airflow velocity fields will be presented in this paper.

The CP section was located 10D downstream of the PIV section. It consisted of two double-wire conductance probes made of platinum. The wires were 0.3 mm thick and separated by 4 mm. Both probes were placed at the centre of the pipe with a distance 6 cm in the stream wise direction. Interface elevation time series were sampled at 500 Hz for approximately 30 minutes.

For more details about the experimental set-up and data processing routines, the reader is referred to [6, 7, 8].

2.1. Wave signal analysis

Local wave parameters, e.g., elevation (η), amplitude (a), length (λ), speed (c), were extracted for each wave cycle, w_n, by means of the zero-crossing method. First, the mean elevation was subtracted from the raw signal given by each probe $\eta_i'(t) = \eta_i(t) - \overline{\eta_i}$. A zero-down-crossing is then defined as the location at which the signal changes sign from positive to negative. Wave crests and troughs are defined as the global maximum and minimum in between two subsequent zero down-crossings, respectively. Probability distributions of any given wave parameter were obtained by means of kernel density estimation [15]. In this paper, exceedance probability distribution (epd) will be evaluated. For more details about this procedure, see [5].

Power spectral densities (PSD) and bicoherence (Bc) will be assessed in the analysis of modal interaction (sec. 3.2). The Bc, here denoted as $\beta(f_j, f_k)$ is a normalized bispectrum, $\phi_{\hat{\eta}\hat{\eta}\hat{\eta}}(f_j, f_k)$. The latter is a triple correlation function in
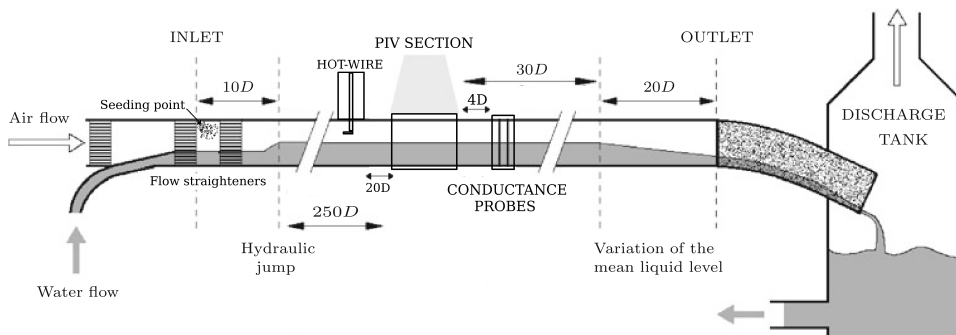

Fig. 1: Schematic view of the experimental setup in use.

the Fourier space which identifies spectral modes that are coherent in phase. The normalization process eliminates any amplitude dependency from the bispectrum. Thus, phase-correlated modes that exactly satisfy the selection criterion $f_1 + f_2 = f_3$ yield $\beta(f_1, f_2) = 1$. The bispectrum and bicoherence are defined as follows (see for instance [29]):

$$\phi_{\hat{\eta}\hat{\eta}\hat{\eta}}(f_j, f_k) = \mathbb{E}\left[\hat{\eta}(f_j)\hat{\eta}(f_k)\hat{\eta}^*(f_j + f_k)\right], \qquad\qquad j, k = 0, 1, ..., M/2 \qquad\qquad (1)$$

$$\beta(f_j, f_k) = \frac{\left|\phi_{\hat{\eta}\hat{\eta}\hat{\eta}}(f_j, f_k)\right|^2}{\mathbb{E}\left[\left|\hat{\eta}(f_j)\hat{\eta}(f_k)\right|^2\right]\mathbb{E}\left[\left|\hat{\eta}^*(f_j + f_k)\right|^2\right]} \qquad\qquad (2)$$

where $\hat{\eta}^*$ is the complex conjugate of $\hat{\eta}$ and M is the sample size of the signal.

Here, the bicoherence was calculated using 250 overlapping widows of 264 points. This choice proved to provide adequate resolution for the bicoherence maps shown in Fig. 5. According to numerical simulations conducted by [25], the minimum significant value of bicoherence required for 95% significance level is given by $\beta_{95\%}^2 \geq 6/N_{im}$, where N_{im} is the number of windows used in the calculation of β. Thus, this threshold was set in our calculations.

2.2. Conditional averaging of PIV velocity fields

From a given PIV image, the interfacial profile was extracted using an intensity-gradient based method. The PIV field of view (FOV) was 90mm wide. This was not enough to fully resolve the spectral peak component, which wave length varied between 1.8 and 2.5 times the FOV, in case A and B, respectively. Nevertheless, by dividing the interface into quadrant and averaging fields over quadrants of similar shape, it was possible to perform meaningful phase-averaging of the velocity fields above the waves. A similar approach was employed by [39] and [12]. However, these studies focused on the water velocity field, i.e., under the interface.

Wave quadrants were identified by means of a zero-crossing procedure. Between two consecutive zero-crossings, global maxima/minima were identified as crests/troughs. The region in between a zero-crossing and a crest/trough was then classified as a wave quadrant according to the definition in figure 2. A minimum wave amplitude of 1 mm was used as a threshold in order to limit the influence of measurement uncertainties close to the interface.

As the interfacial elevation consists of a spectrum of wave components with varying heights, lengths and steepnesses, a criteria is employed prior to averaging. The wave steepness is known to have a significant impact on the airflow above waves, affecting the critical layer height and the streamline pattern above the waves [22]. For this reason, wave steepness was chosen as the averaging criterion in this study. Conditional averaging based on wave steepness was also performed by [2], in investigating the velocity field in the liquid phase below 2D millimetre-scale waves.

The airflow domain was subjected to a coordinate transformation from Cartesian coordinates (x, y) to wave-following coordinates (θ, ζ). The crest, trough and zero crossings were assigned phases of $0°$, $180°$ and $+/- 90°$, respectively (see figure 2), whilst phases in between were linearly distributed. The vertical coordinate $\zeta = (y - \eta(x))/\eta_c$ is the dimensionless distance from the interface, normalized by the crest amplitude. The resulting coordinate system is illustrated in figure 2 for a single Q2 observation. The velocity fields above the identified wave quadrants are sampled from $\zeta = 0$ to 5. For each quadrant observed, all variables of the flow field (u, v, vorticity etc.) were sampled at the equally distributed (θ, ζ) coordinates, with 180 points in the θ direction and 100 points ζ direction. More details about this phase-averaging procedure may be found in [44].
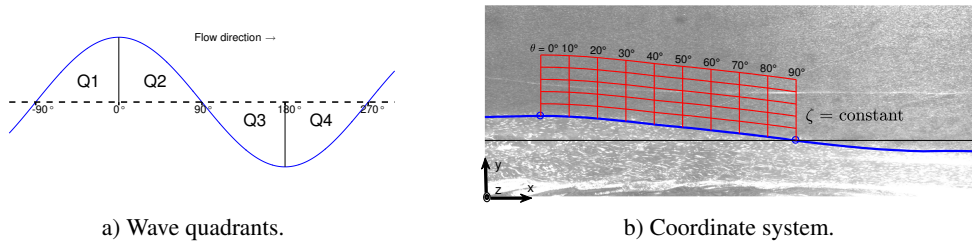
a) Wave quadrants.   b) Coordinate system.

Fig. 2: Left: Definition of quadrants. Dotted line represents mean water level. x-axis represents the wave phase. Right: Example of an identified quadrant (Q2 event), and wave following coordinate system above the wave quadrant. Note that in the laboratory frame of reference, the x-axis is in the flow direction, y points upwards, while z goes out of the $x - y$ plane.

3. Results

The cases under investigation in this study are depicted amongst a larger data bank. Some important parameters concerning these cases are listed in Table 1. Figure 3 shows the evolution of RMS amplitude normalized by the pipe diameter σ_η/D, as well as the steepness (ak) of the most probable wave as a function of increasing gas superficial velocity U_{sg}. Both cases under investigation are shown as red squares. Note that in all cases shown in the figure, the liquid superficial velocity was kept constant at 0.1m/s. The corresponding bulk velocity varied between 0.24 and 0.32 m/s. This variation is dictated by conservation of mass in a confined space, i.e., as the gas flow rate increases, the liquid level decreases (from 0.45D to 0.37D) and thus the liquid bulk velocity increases.

The first measurable waves appeared at air velocity $U_{sg} \approx 1$ m/s. At velocities up to $U_{sg} \approx 1.7$ m/s, the waves grow, both in height and length. The relative growth in height is greater than the corresponding growth in length. Thus, the average wave steepness also with increasing gas velocity. Above $U_{sg} \approx 1.7$, the RMS amplitude stabilizes around 2.3 mm, while the steepness oscillates around 0.13. Note that these values stem from the conductance probe measurement and differ slightly from PIV measurements taken slightly upstream [44]. Based on available data, one may claim that the evolution wave amplitudes can be categorized into two regimes; i) wave growth regime in which case A features, and ii) wave saturation regime which includes case B. Note that in both cases under investigation, the effective wave speed $(c - U_{bl})$ is well described by the dispersion relation for finite depth gravity waves, see [7].

Exp. case	U_{sl} [m/s]	U_{sg} [m/s]	U_{bl} [m/s]	U_{bg} [m/s]	Re_{Dg} [-]	Re_{Dl} [-]	σ_η/D [-]	c [m/s]	λ_p/D [-]	$\overline{h_w}/D$ [-]	c/u_* [-]
A	0.1	1.5	0.26	2.44	11 238	25 167	0.7%	0.71	0.25	0.41	2.1
B	0.1	2.1	0.26	3.49	15 793	24 921	2.2%	0.81	2.1	0.42	2.7

Table 1: Characteristics of experimental cases under investigation.

3.1. Statistical characterization of interfacial waves

In both cases A and B, the interfacial waves display rather random behaviour to the naked eye. Although it is possible to visually identify a dominant mode, figure 5 reveals that the spectral content is relatively broad-banded and multimodal. Thus in order to categorize the wavy regimes, we evaluate the statistical properties of each elevation time series and use the Gaussian wave model as a reference, see for instance [35] for a review on Gaussian wave statistics. To this end, exceedance probability distributions of the elevation time series $\eta(t)$ and the Hilbert upper envelope $A_{up}(t)$ are compared to their associated Gaussian and Rayleigh distributions, respectively, in figure 4.

With small discrepancies at the tails, the exceedance distribution of case A is well described by Gaussian statistics. This means that the wave field consists of a linear superposition of statistically independent Fourier modes. It is thus reasonable to categorize the waves in case A within a "linear regime" in which non-linear contributions are negligible. Case B, however, deviates significantly from linear Gaussian theory. In contrary to rogue ocean surface waves for which Gaussian statistics is expected to underestimate the most extreme waves, both the normal and Rayleigh dis-

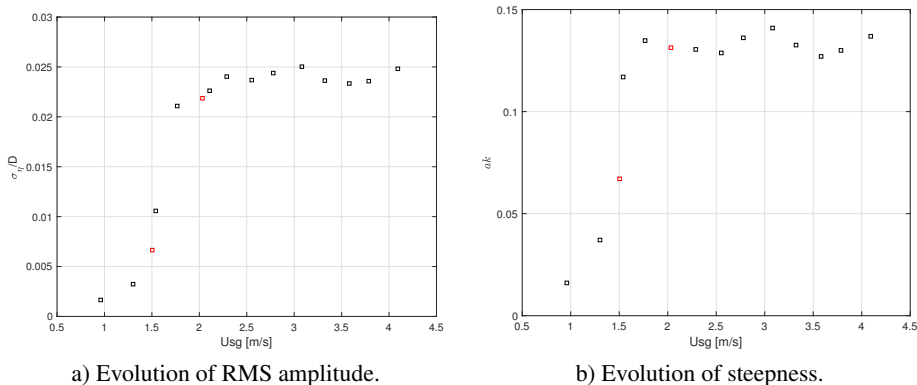| a) Evolution of RMS amplitude. | b) Evolution of steepness. |

Fig. 3: Evolution of RMS amplitude σ/D and steepness ak with increasing gas velocity. Note that the two cases under detailed investigation are depicted by red squares.

tributions strongly overestimate the exceedance distributions of measured elevation and upper envelope, respectively. This is especially the case in the tail region of the exceedance distributions, i.e., at $y/\sigma > 2$. This means that the wave field does not contain large amplitude waves which are expected to be present on a Gaussian surface. However, by closer investigation, it appears that the exceedance distribution of A_{up} first overshoots above the Rayleigh distribution for y-values up to 1.8σ, before undershooting.

This behaviour is attributed to non-linear effects. Most likely, the dominant (and most common) wave grows by means of energy transfer through non-linear wave interaction and wind input, becomes too steep and subsequently breaks. It is worthwhile emphasizing that wave breaking with air entrainment was not observed during the experimental campaign. However, weaker forms of breaking such as spilling or micro-breaking is very likely to have taken place, although this cannot be affirmed by means available experimental data. This is in fact the subject of an ongoing study.

In order to assess modal interaction, power spectral densities and bicoherence maps are analysed in the following section.
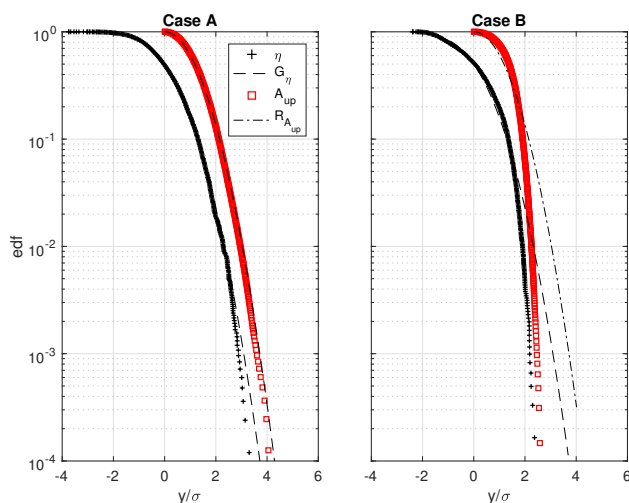

Fig. 4: Exceedence distribution of the wave elevation η and Hilbert upper envelope A_{up}, here normalized by the elevation standard deviation. The associated Gaussian (black dashed line) and Rayleigh (red dashed line) distributions are plotted for comparison.

3.2. Spectral analysis and modal interaction

Power spectral densities shown in figure 5 reveal that both cases have spectral peaks at $f \approx 4$ and 8 Hz. In addition, case B has a third peak at 10 Hz. The 8 Hz mode is likely to be the fundamental mode of this system. It is associated with the first measurable waves that appear at $U_{sg} \approx 1$ m/s (not shown here), see [7]. Their wavelength is approximately half the water depth and their measured celerity is $c \approx 20$ cm/s, which corresponds to the phase speed of gravity-capillary waves. The sub-harmonic mode at ~4 Hz appears once the gas velocity exceeds 1.30 m/s. This mode has a dominant wavelength $\lambda \approx 2D$ and lies on the gravity side of the dispersion relation [13]. It seems likely that this mode results from sub-harmonic bifurcation ($2 \rightarrow 1$), also called period doubling [27]. As the gas velocity increases, the sub-harmonic mode grows and experiences a slight frequency downshift [41, 31, 21], as can be seen in figure 5.

Period doubling is characterized by fast energy transfer from the fundamental to the sub-harmonic mode [27]. Campbell and Liu [18] considered the role of non-linear sub-harmonic resonant wave interaction in the development of interfacial waves. They found that the sub-harmonic mode receives energy from its linearly unstable fundamental mode at a faster than exponential rate. Meanwhile, in his reassessment of Chen and Saffman's experiments [20], Janssen [27] argued that in real wind-wave systems, one should expect a quasi-resonant sub-harmonic interaction since wind induces relatively broad-banded disturbances. Thus, one should expect that the rate of energy transfer is relatively lower than reported by [18]. Our observations are in agreement with Janssen's argument. Some 5 m upstream of the measurement set-up, it was possible to observe the period-doubling process taking place over a distance of approximately 1 m. By increasing the gas velocity, the location at which the period doubling takes place was shifted further upstream, i.e., higher gas velocity accelerates the process of bifurcation. To this end, at even higher gas velocities than case B, the 4 Hz mode has had both more time and space to develop before reaching the test section.

The bicoherence plots in figure 5 reveal that in case A, there is only sign of overtone coupling emerging from interaction of the fundamental 8 Hz mode with itself giving rise to a noticeable small peak at 16 Hz in the power spectrum. Note that the bicoherence peak is at slightly higher frequency (~ 9 Hz) that the spectral peak. The 16 Hz disturbances are most likely to remain stable as these are capillary waves governed by surface tension. However, this part of the spectrum contributes to the surface roughness. It is interesting to note that the bicoherence map shows no sign of interaction related to sub-harmonic mode at 4 Hz. It is as if this mode behaves as a free wave. Further investigation is needed to draw any conclusion regarding this observation.

In case B, the bicoherence plot indicates the presence of both overtone interaction, $\beta(4Hz, 4Hz)$ and $\beta(8Hz, 8Hz)$, as well as sub-harmonic interaction $\beta(8Hz, 4Hz)$, in addition to contributions from lower frequency modes (2Hz). These large scale fluctuations are believed to increase the irregularity of the wave field. In both cases, the peak bicoherence is related to the overtone interaction of the peak mode with itself, i.e., $\beta(8Hz, 8Hz)$ in case A and $\beta(4Hz, 4Hz)$ in case B.
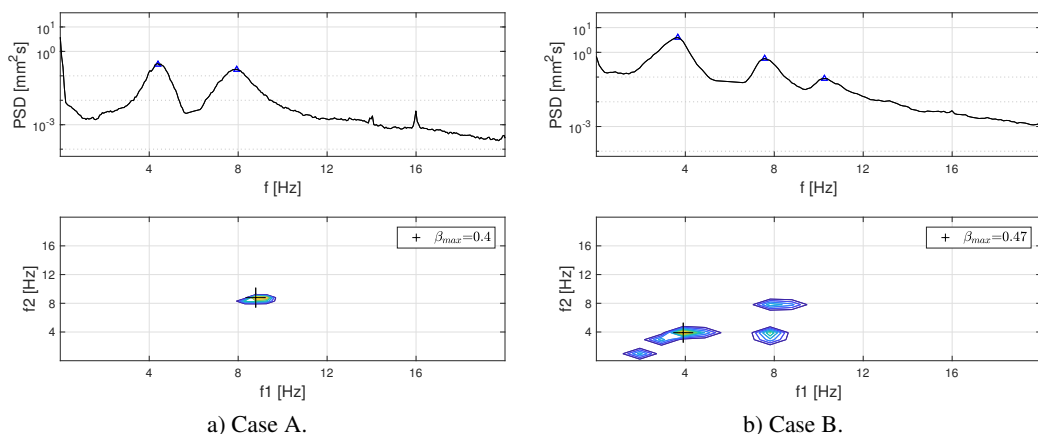

a) Case A.   b) Case B.

Fig. 5: PSD and bicoherence map for cases A and B. The '+' sign indicates the peak bicoherence.

In their study of interfacial gravity-capillary waves in horizontal gas-liquid flows, Jurman et al. [29] attributed the observed saturation of wave amplitudes to non-linear energy transfer from unstable to stable modes. Nevertheless, their study did not include any assessment of the flow field above the waves. Recent experimental and numerical studies on turbulent airflow above propagating waves [17, 45] have reported evidence of intermittent airflow separation events above steep non-breaking waves. Airflow separation introduces a velocity discontinuity above the wave trough region, which reduces the momentum transfer between the phases. This phenomenon is therefore expected to play a role in the saturation of wave amplitudes discussed above. In the next section, the structure of airflow is assessed by means of the conditional-averaging procedure outlined in section 2.2.

3.3. Structure of the airflow

Streamlines of the phase-averaged airflow field, seen in a frame of reference moving with the mean wave speed, are plotted for cases A and B in figure 6. The critical height $y_c(\theta)$, i.e., the height at which $U_g(y) = \bar{c}$, is represented by a dashed black line. The viscous sublayer thickness ($y_{vs} = 5\nu_g/u_*$), is shown by a red dashed line. It is normalized by the average crest height η_c in each case. In case A, $y_{vs} = 0.24$ mm $= 0.12\eta_c$, whilst in case B $y_{vs} = 0.25$ mm $= 0.05\eta_c$.

In case A, the critical layer follows the shape of the average wave profile. For the most part, the critical layer lies within the viscous sublayer. However, $y_c(\theta)$ is slightly larger on the lee side of the crest ($0° < \theta < 150°$) compared to its windward side. This is because the airflow velocity is marginally lower in the trough region. Nevertheless, compared to case B, $y_c(\theta)$ is rather symmetric about the crest. The phase-averaged streamlines also follow the shape of the wave surface except near the critical height at $\theta = 100°$ and $180°$, where two small region of enclosed streamlines can be depicted.

In case B, the critical layer is adjacent to the surface at $-50° < \theta < 0°$, whilst in the trough region, its height is comparable to the average crest amplitude, i.e., $y_c(\theta > 0°) \sim \eta_c$. Overall, the critical layer height lies substantially far above the viscous sublayer, indicating that the former plays an important role in the development of the waves. The asymmetry in $y_c(\theta)$ is a result of sheltered airflow in this region. Whether this sheltering process implies airflow separation [28] or not (non-separated sheltering [11]), depends on the temporal frame of reference applied to view the flow. In some instantaneous flow fields, there were clear signs of separated streamlines (not shown), with detachment and reattachment points. These features are not seen in the phase-averaged streamlines shown in fig. 6. Nevertheless, a large region of enclosed streamlines "cat's eye" can be seen slightly downstream of the crest ($\theta = 50°$). The position of this "eye" implies that, on average, a wave experiences a co-moving pocket of air located slightly downwind of its crest, thus altering the pressure distribution around the crest.

Hara and Sullivan [24] performed large eddy simulation of strongly forced young waves ($c/u_* = 1.6$) with wave steepness $ak = 0.226$, i.e., a regime which is qualitatively comparable to case B. Their results showed that an asymmetric critical height implies asymmetry in pressure distribution above the wave. The peak pressure moves downstream from the wave towards to the windward side of the next wave. This results in a flux of horizontal momentum locally, pushing the wave in the flow direction. Although we do not have measurements of the pressure field, it is reasonable to assume that similar scenario takes place in case B.
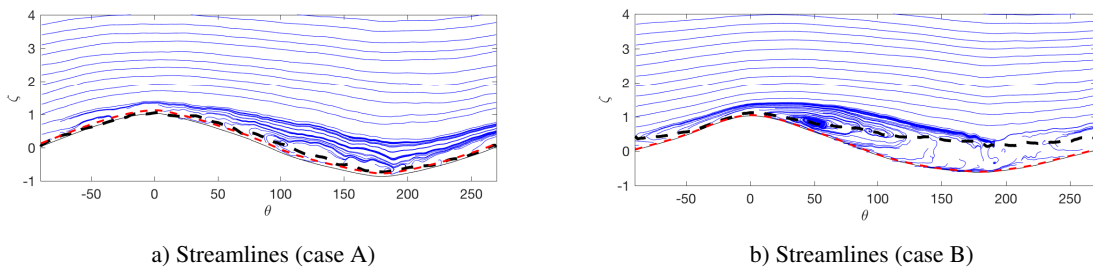

a) Streamlines (case A)　　　　　　　　b) Streamlines (case B)

Fig. 6: Streamlines of $\boldsymbol{u} - \bar{c}$ for averaged flow field. The critical layer height $y_c(\theta)$ is shown by the dashed black line, whereas the red dashed line indicates the viscous sublayer thickness $y_{vs} = 5\nu_g/u_*$.

Isolated swirling structures in any given instantaneous velocity field were identified by means of the swirling strength criterion (λ_{ci}), see [1] for a review of this method. Figure 7 shows selected instantaneous fields from case A

and B. Both were chosen because they contained a crest of the left side of the PIV-image, thus showing the swirling field downstream of a crest. The figures reveal that as the air flows past a crest, there is a remarkable shedding of negative swirling motion. Note that negative rotation axis points inwards in the (x, y)-plane. The shed vortices in case B are visibly more intense than in case A. This is a consequence of the air velocity being larger and the wave steeper than in case A. Such zones of recirculating airflow have been described by Hunt and Sajjadi [26] for flow above growing wave trains.
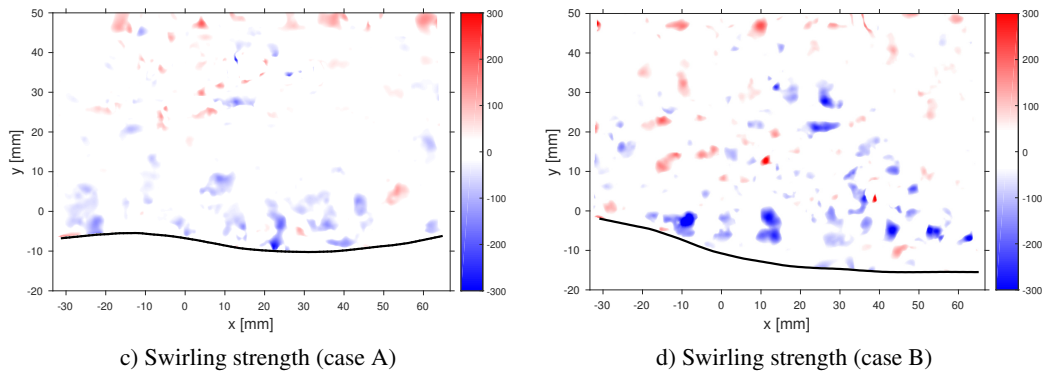

c) Swirling strength (case A)   d) Swirling strength (case B)

Fig. 7: Instantaneous swirling strength fields (λ_{ci}-criterion [1]) past wave crests. Blue colour indicates negative swirling (rotation axis inward in the plane), while red indicates positive swirling.

The phase-averaging routine described earlier was applied on instantaneous swirling strength fields. The result is shown in figure 8. This figure is closely related to a phase-averaged vorticity field. It can be seen from the figure that a layer of negative vorticity remains adjacent to average wave surface in case A. In case B, the equivalent layer separates from the interface at $\theta \approx 25°$. This separation takes place at the same location at which the critical layer detaches from the surface. In this case, the criterion for shear-layer separation as defined by Buckley and Veron [17] is fulfilled. It can be noted that below the critical height there is a region dominated by positive vorticity, i.e., opposite direction of the vorticity present in the separated shear layer. This particular phenomenon is expected to lower the rate of vertical momentum transfer contributing to wave growth and thus be a partial cause for the observed amplitude saturation seen in figure 3. Nevertheless, at this stage, we do not attempt to quantify the effect of this process, as this is the subject of an ongoing study in which phase-locked PIV is conducted in order to obtain considerably larger sets of relevant data.
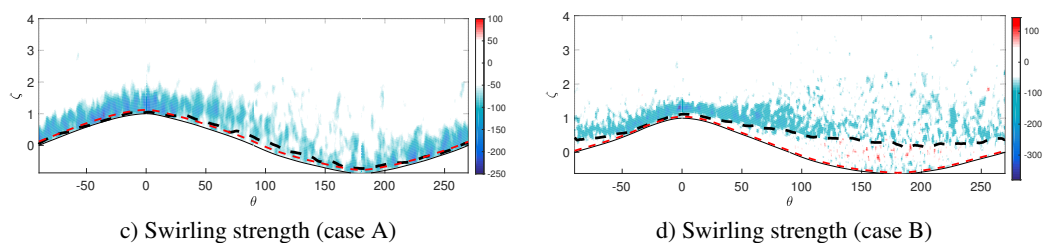

c) Swirling strength (case A)   d) Swirling strength (case B)

Fig. 8: Phase-averaged swirling strength fields $\langle\lambda_{ci}\rangle$. Black dashed line represents the critical height, while the viscous sublayer is depicted by the red dashed line.

4. Concluding remarks

We have studied stratified gas-liquid flow experimentally using PIV and conductance probes. Two cases, in which the air bulk velocity increased from 2.4 m/s to 3.5 m/s while the liquid velocity was kept constant at 0.26 m/s, were studied in detail. Case A belongs to a region of flow conditions in which wave amplitudes grow as a consequence of increasing gas flow rates, i.e. growth regime. Meanwhile, case B is in a regime of saturated wave amplitudes.

One of the main goals of this phenomenological study was to categorize the interfacial waves using statistical and spectral methods. We observed that the small amplitude waves present in case A behaved according to Gaussian statistics. This was portrayed by good agreement between the exceedance probability distributions of the wave elevation η and the upper envelope A_{up} with their associated Gaussian and Rayleigh distributions. However, case B showed significant deviation from Gaussian statistics, as both the normal and Rayleigh distributions over-predicted measured exceedance in the tail region. This signifies that large amplitude waves which are expected to be present on a Gaussian surface are suppressed. This behaviour is attributed to non-linear modal interactions that left their mark on bicoherence maps shown in section 3.2. In addition, micro-breaking or spilling was mentioned as an other potential explanation for these deviations.

In the second part of the paper, the structure of airflow above waves in cases A and B was investigated by means of a conditional averaging method applied to the PIV velocity fields. The reason for performing this analysis was to study the influence of two different wave regimes on the airflow, and also to determine whether any form of flow separation takes place. Phase-averaged streamlines showed that a noticeable region of enclosed streamlines (cats eye) was present in case B. Here, the critical layer was distributed asymmetrically about the wave crest, implying asymmetric pressure distribution as described by [24]. An analysis of coherent vortices present in instantaneous airflow snapshots revealed that wave-shed (negative) vortices were more intense in case B as a result of higher air velocity and wave steepness.

The phase-averaged vorticity field in case B showed clear signs of shear-layer separation immediately downstream of the crest. The separated shear layer was found to follow the critical layer. The critical layer itself was dominated dominated by counter-rotating (positive) vortices. Above the average wave of case A, which is less steep than in case B, no signs of separation was found. Here, the negative vorticity layer stayed adjacent to the surface, as too did the critical layer. Thus, one may conclude that as shear-layer separation occurs in the saturation regime. This phenomenon should probably be taken into consideration in attempts to explain the observed transition to the saturated wave amplitude regime.

It was not within the scope of this study to quantify the effect of the above mentioned processes, as this was merely a qualitative study. However, this study has functioned as a foundation for an ongoing experimental campaign in which the aim is to quantify the effect of, amongst other processes, flow separation and micro-breaking.

Acknowledgements

References

1. Adrian, R., 2007. Hairpin vortex organization in wall turbulence. Phys. Fluids 19.
2. André, M.A., Bardet, P.M., 2017. Viscous stress distribution over a wavy gas–liquid interface. International Journal of Multiphase Flow 88, 1–10.
3. Andreussi, P., Persen, L., 1986. Stratified gas-liquid flow in downwardly inclined pipes. I. J. Multiphase flow 13, 565–575.
4. Andritsos, N., Hanratty, T., 1987. Influence of interfacial waves in stratified gas-liquid flows. AIChE Journal 33, 444–454.
5. Ayati, A., Carneiro, J., 2018. Statistical characterization of interfacial waves in turbulent stratified gas-liquid pipe flows. Int. Journal of Multiphase Flow (in press) .
6. Ayati, A., Kolaas, J., Jensen, A., Johnson, G., 2014. A PIV investigation of stratified gasliquid flow in a horizontal pipe. International Journal of Multiphase Flow 61, 129 – 143.
7. Ayati, A., Kolaas, J., Jensen, A., Johnson, G., 2015. Combined simultaneous two-phase PIV and interface elevation measurements in stratified gas/liquid pipe flow. International Journal of Multiphase Flow 74, 45 – 58.
8. Ayati, A., Kolaas, J., Jensen, A., Johnson, G., 2016. The effect of interfacial waves on the turbulence structure of stratified air/water pipe flow. International Journal of Multiphase Flow 78, 104 – 116.
9. Barmak, I., Gelfgat, A., Vitoshkin, H., Ullmann, A., Brauner, N., 2016. Stability of stratified two-phase flows in horizontal channels. Physics of Fluids 28, 044101.
10. Barnea, D., Taitel, Y., 1993. Kelvin-Helmholtz stability criteria for stratified flow: viscous versus non-viscous (inviscid) approaches. I. J. Multiphase Flow 19, 639–649.
11. Belcher, S., Hunt, J., 1993. Turbulent shear flow over slowly moving waves. Journal of Fluid Mechanics 251, 109–148.

12. Birvalski, M., Tummers, M., Delfos, R., Henkes, R., 2014. PIV measurements of waves and turbulence in stratified horizontal two-phase pipe flow. I.J. of Multiphase Flow 62, 161–173.

13. Birvalski, M., Tummers, M.J., Delfos, R., Henkes, R., 2015. Laminar-turbulent transition and wave-turbulence interaction in stratified horizontal two–phase pipe flow. Journal of Fluid Mechanics 780, 439–456.

14. Bontozoglou, V., Hanratty, T., 1990. Capillary-gravity Kelvin-Helmholtz waves close to resonance. Journal of Fluid Mechanics 217, 71–91.

15. Bowman, A.W., Azzalini, A., 1997. Applied smoothing techniques for data analysis: the kernel approach with S-Plus illustrations. volume 18. OUP Oxford.

16. Bratland, O., 2010. Pipe flow 2 multi-phase flow assurance. Chapt 18, 274–284.

17. Buckley, M.P., Veron, F., 2016. Structure of the airflow above surface waves. Journal of Physical Oceanography 46, 1377–1397.

18. Campbell, B.K., Liu, Y., 2014. Sub-harmonic resonant wave interactions in the presence of a linear interfacial instability. Physics of Fluids 26, 082107.

19. Campbell, B.K., Liu, Y., 2016. A nonlinear flow-transition criterion for the onset of slugging in horizontal channels and pipes. Physics of Fluids 28, 082103.

20. Chen, B., Saffman, P., 1979. Steady gravity–capillary waves on deep water–1. Weakly nonlinear waves. Studies in Applied Mathematics 60, 183–210.

21. Eeltink, D., Lemoine, A., Branger, H., Kimmoun, O., Kharif, C., Carter, J., Chabchoub, A., Brunetti, M., Kasparian, J., 2017. Spectral up-and downshifting of akhmediev breathers under wind forcing. Physics of Fluids 29, 107–103.

22. Gent, P., Taylor, P., 1977. A note on separationover short wind waves. Boundary-Layer Meteorology 11, 65–87.

23. Grare, L., Peirson, W.L., Branger, H., Walker, J.W., Giovanangeli, J.P., Makin, V., 2013. Growth and dissipation of wind-forced, deep-water waves. Journal of Fluid Mechanics 722, 5–50.

24. Hara, T., Sullivan, P.P., 2015. Wave boundary layer turbulence over surface waves in a strongly forced condition. Journal of Physical Oceanography 45, 868–883.

25. Haubrich, R.A., 1965. Earth noise, 5 to 500 millicycles per second: 1. spectral stationarity, normality, and nonlinearity. Journal of Geophysical Research 70, 1415–1427. Significant bicoherence threshold.

26. Hunt, J., Sajjadi, S., 2018. Mechanisms and modelling of wind driven waves. Procedia IUTAM .

27. Janssen, P.A.E.M., 1986. The period–doubling of gravity–capillary waves. Journal of Fluid Mechanics 172, 531–546.

28. Jeffreys, H., 1925. On the formation of water waves by wind, in: Proc. R. Soc. Lond. A, The Royal Society. pp. 189–206.

29. Jurman, L., Deutsch, S., McCready, M., 1992. Interfacial mode interactions in horizontal gasliquid flows. Journal of Fluid Mechanics 238, 187–219.

30. Kaffel, A., Riaz, A., 2015. Eigenspectra and mode coalescence of temporal instability in two-phase channel flow. Physics of Fluids 27, 042101.

31. Kharif, C., Giovanangeli, J.P., Touboul, J., Grare, L., Pelinovsky, E., 2008. Influence of wind on extreme wave events: experimental and numerical approaches. Journal of Fluid Mechanics 594, 209–247.

32. Lakehal, D., Fulgosi, M., Banerjee, S., Angelis., D., 2003. Direct nnumerical simulation of turbulence in a sheared air water flow with a deformable interface. J. Fluid Mech 482, 319–345.

33. Mata, C., Pereyra, E., Trallero, J., Joseph, D., 2002. Stability of stratified gas–liquid flows. International journal of multiphase flow 28, 1249–1268.

34. Miles, J., 1957. On the generation of surface waves by shear flows. I. J. of Multiphase flow 3, 185–204.

35. Onorato, M., Residori, S., Bortolozzo, U., Montina, A., Arecchi, F., 2013. Rogue waves and their generating mechanisms in different physical contexts. Physics Reports 528, 47 – 89.

36. Phillips, O., 1957. On the generation of waves by turbulent wind. J. Fluid Mech. 2, 417–445.

37. Pothof, I., Clemens, F., 2011. Experimental study of air–water flow in downward sloping pipes. International Journal of Multiphase Flow 37, 278 – 292.

38. Shoham, O., Taitel, Y., 1984. Stratified turbulent-turbulent gas-liquid flow in horizontal and inclined pipes. AIChE journal 30, 377–385.

39. Siddiqui, K., Loewen, M.R., 2010. Phase-averaged flow properties beneath microscale breaking waves. Boundary-Layer Meteorology 134, 499–523.

40. Taitel, Y., Dukler, A., 1976. A theoretical approach to the Lockhart–Martinelli correlation for stratified flow. I.J. Multiphase Flow 2, 591–595.

41. Trulsen, K., Dysthe, K.B., 1992. Action of wind stress and breaking on the evolution of a wave train, in: Breaking Waves. Springer, pp. 243–249.

42. Tzotzi, C., Andritsos, N., 2013. Interfacial shear stress in wavy stratified gas–liquid flow in horizontal pipes. I. J. Multiphase Flow 54, 43 – 54.

43. Ullmann, A., Brauner, N., 2006. Closure relations for two-fluid models for two-phase stratified smooth and stratified wavy flows. International journal of multiphase flow 32, 82–105.

44. Vollestad, P., Ayati, A.A., Angheluta, L., LaCasce, J.H., Jensen, A., 2018. Analysis of airflow above waves in pipes using conditionally averaged piv. Under review at Journal of Fluid. Mech. .

45. Yang, D., Shen, L., 2010. Direct-simulation-based study of turbulent flow over various waving boundaries. Journal of Fluid Mechanics 650, 131–180.